論文 / 著書情報
Article / Book Information

Title	Simulation-based study on a dual-circuit design for achieving continuous power generation in Ge-sensitized thermal cells under isothermal conditions
Authors	Keting Chen, Mie Tohnishi, Akihiro Matsutani, Sachiko Matsushita
Citation	Energy Conversion and Management, Volume 331, , Page 119678
Pub. date	2025, 5
DOI	https://dx.doi.org/10.1016/j.enconman.2025.119678
Creative Commons	Information is in the article.

Energy Conversion and Management 331 (2025) 119678

Contents lists available at ScienceDirect

Energy Conversion and Management

journal homepage: www.elsevier.com/locate/enconman

Research Paper

Simulation-based study on a dual-circuit design for achieving continuous power generation in Ge-sensitized thermal cells under isothermal conditions

Keting Chen [a], Mie Tohnishi [b], Akihiro Matsutani [b], Sachiko Matsushita [a,c,*]

[a] Department of Materials Science and Engineering, Institute of Science Tokyo, J2Bldg.1410, 4259 Nagatsuta, Midori-ku, Kanagawa 226-8503, Japan
[b] Core Facility Center, Institute of Science Tokyo, R1Bldg.A203, 4259 Nagatsuta, Midori-ku, Kanagawa 226-8503, Japan
[c] elleThermo, Ltd, INDEST 3F, Institute of Science Tokyo, Shibaura 3-3-6, Minato-ku, Tokyo 108-0023, Japan

ARTICLE INFO

Keywords:
Thermoelectric
Thermal energy conversion
Renewable energy
Dye-sensitized solar cell
Comb electrodes
Interdigitated array electrodes
Semiconductor

ABSTRACT

The semiconductor-sensitized thermal cell (STC) is a groundbreaking thermoelectric technology capable of converting low-temperature heat (<200 °C) directly into electricity. It is based on a redox reaction initiated by thermally excited carriers in a semiconductor. One of its most appealing features is that once the STC reaches discharge termination, power generation can be restored by turning off the switch and leaving it in the heat source. However, during this recovery period, no power is generated, which significantly affects the efficiency of the STC system. To address this issue, this study proposes a dual-circuit STC model utilizing interdigitated array (IDA) electrodes, designed to eliminate recovery time and enable continuous power generation by alternating between two circuits within a single STC. Simulation and experimental methods were employed to assess the performance of this model. Two-dimensional (2D) simulations of the battery structure confirm that circuit switching triggers the redox reaction in the alternate circuit with sufficient reactant ions, enabling continuous discharge. Experimental results validate the continuous power generation observed in the fabricated cells. The dual-circuit system achieves an open circuit voltage Voc of approximately 270 mV (for both circuits) and a short circuit current Isc of around 0.30 μA (Jsc of 5 μA/cm^2), demonstrating significant potential for application in IoT devices.

1. Introduction

Heat, often considered low-quality energy owing to substantial losses inherent in energy conversion processes, represents a significant challenge globally, with more than half of produced energy dissipating into the environment as waste heat [1]. As energy demand rises, finding efficient ways to use waste heat and generate electricity from natural heat sources becomes increasingly critical. Geothermal power generation is the predominant technology for harnessing heat to produce electricity [2]. This method involves using heat to generate steam for driving turbines. Another thermoelectric conversion approach relies on the Seebeck effect [3], where a voltage is generated across dissimilar conductors or semiconductors owing to a temperature difference. Recent studies have explored various strategies to enhance the performance of thermoelectric generators (TEGs) based on this principle. Luo et al. (2024) [4] developed a flexible micro-TEG with a Y-type TE unit design, leading to a 44 % increase in power compared to the original design. Toan et al. (2025) [5] investigated how nanoporous silicon reduces thermal conductivity and significantly improves the Seebeck coefficient. These advancements highlight ongoing efforts to optimize TEGs for practical applications. However, geothermal power generation requires substantial water resources, and a cooling system is always essential for applications using the Seebeck effect.

Recently, thermoelectric conversion without relying on temperature gradients has gained considerable attention as a field of active research. Kondo, S. et al. (2024) [6] reported an organic thermoelectric device capable of achieving isothermal power generation through the charge separation properties of organic charge transfer (CT) interfaces. This paper focuses on another thermoelectric device using semiconductors, which offers a simpler module design.

Semiconductor-sensitized thermal cell (STC) is an attractive technology which is capable to harvest electricity directly from low-

* Corresponding author.
E-mail address: matsushita.s.ab@m.titech.ac.jp (S. Matsushita).

https://doi.org/10.1016/j.enconman.2025.119678
Received 23 October 2024; Received in revised form 11 February 2025; Accepted 23 February 2025
Available online 1 March 2025

temperature heat [7–17]. Current STCs can reliably achieve power output in the microwatt range between room temperature and 80 °C [15], are well-suited for small IoT devices, such as pedometers, glucose sensors, and pressure sensors, that operate within the nanowatt (nW) to microwatt (μW) range [18]. A series of four STC coin cells successfully powered a battery-less wireless sensor on asphalt, generating a Bluetooth signal that was detected by a smartphone [15]. Additionally, by connecting multiple STCs in series, their voltage output can be increased. A previous study demonstrated that an origami-structured array of 12 STCs at 60 °C powered a liquid crystal display, achieving an output of 0.9 V [10]. This scalability underscores their potential for real-world applications.

The mechaism of STC was inspired by dye-sensitized solar cells (DSSCs) [19–21], which generate electricity through photoexcitation of electrons by light. Instead, STCs operate via redox reactions triggered by thermally excited electrons in semiconductors. The structure and operation of the STC are illustrated in Fig. 1. When heat is applied to the STC, lattice vibrations thermally excite electrons in the semiconductor. These excited electrons travel through the electron transport layer and external circuit to the counter electrode. Subsequently, these transferred electrons facilitate oxidation and reduction reactions of electrolyte ions, thereby generating an electric current.

As a battery, the STC naturally reaches a discharge endpoint. There are two primary reasons for this termination: (1) insufficient ions to sustain redox reactions and (2) reaching chemical equilibrium [16]. Remarkably, one of the most appealing features of the STC is that power generation can be restored simply by turning off the switch and leaving it in the heat source. This recovery occurs because opening the discharge cell's circuit causes a redistribution of ions, eventually reaching a new equilibrium that allows for renewed discharge. Here, to prevent any misunderstandings, the terms "recovery time" and "redischarge" are redefined in this paper as follows:

−Recovery time: The time during which the STC is left in an open-circuit state inside the heat source after the previous discharge has ended.

−Redischarge: The ability of the STC to restore its open-circuit voltage to its original value after the recovery time, allowing for subsequent discharge.

These definitions will be consistently used throughout the paper.

The power generation of STCs utilizing organic-perovskite [8], β-$FeSi_2$ [12], and Ag_2S [9] has been confirmed in previous studies. More recently, STCs with a Ge semiconductor working electrode (Ge–STC) and Cu^+/Cu^{2+} redox species have been extensively studied. These Ge–STCs exhibit more stable performance and power generation at approximately 80 °C [10], while also showing the potential to generate power at lower temperatures near room temperature. The structure of Ge–STC can generally be categorized into two types: (1) the conventional sheet type (Fig. 2a), where the electrolyte is sandwiched between substrates, and (2) the comb-type or IDA electrode type (Fig. 2b), where the working and counter electrodes intersect and are printed on a single substrate (Fig. 2e).

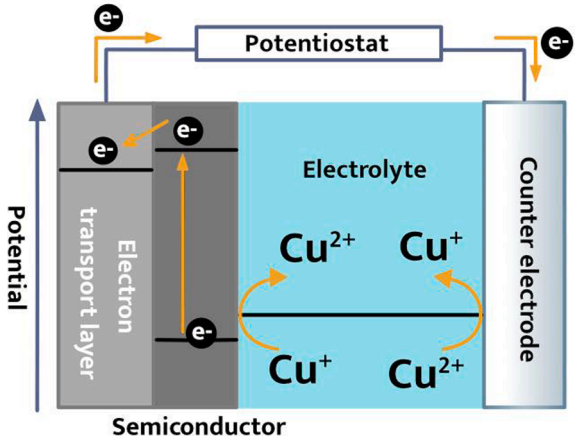

Fig. 1. Schematic diagram of STC.

During STC operation, the assumed distribution of Cu^+/Cu^{2+} in the electrolyte is depicted in Fig. 2 below each STC structure, using different colors to denote ion species (light yellow for Cu^+, dark blue for Cu^{2+}). Initially, when the switch is turned off, the redox species in the electrolyte are uniformly distributed. Upon switching on, the Ge–STC initiates discharge through reactions (1) and (2):

$$\text{Working electrode (Ge): } Cu^+ \rightarrow Cu^{2+} + e^- \quad (1)$$

$$\text{Counter electrode (Pt): } Cu^{2+} + e^- \rightarrow Cu^+ \quad (2)$$

A bias in the distribution of Cu^+/Cu^{2+} begins to develop. Once discharge reaches its endpoint, turning off the switch again prompts the biased ions to diffuse back. This diffusion eliminates the ion concentration gradient in the electrolyte, restoring it to its original equilibrium state—a unique recovery process of STC. The ion diffusion rate during recovery is closely linked to the distance between electrodes. Therefore, the IDA electrode type STC exhibits faster ion diffusion and a shorter recovery because the electrode distance is significantly smaller than the sheet type STC [15].

In previous studies, a recovery process has been considered necessary for a cell to redischarge, regardless of its duration. During this recovery period, no power is generated, which significantly affects the efficiency of the STC system. However, the optimization of this recovery process has not been fully addressed, and its effect on the overall system performance remains a challenge. To overcome this issue, a novel dual-circuit STC model (Fig. 2c) is proposed in this research, designed to potentially eliminate the recovery time by alternating between circuits. Images of the STCs are depicted in Fig. 2d. The newly designed STC consists of two sets of IDA electrodes arranged facing each other and sandwiching an electrolyte. Each IDA electrode (Fig. 2e) features Ge (thickness: 1 μm) as the working electrode and Pt (thickness: 0.05 μm) as the counter electrode, with a 20 μm distance between them and an electrode width of 10 μm. As shown in Fig. 2c, the STC contains two circuits in a single cell, thus earning the designation 'dual-circuit STC'. Given that Ge–STC operates through a Cu^+/Cu^{2+} redox reaction, the design facilitates the reverse reaction on the side with ample ion supply once discharge completes in one circuit. Therefore, if there is a sufficient supply of reactant ions, the oxidation–reduction reaction can continue in the alternate circuit, enabling the continuous discharge of the battery.

Software modeling and two-dimensional (2D) simulations are employed to analyze ion concentration distribution in the electrolyte. The simulation results demonstrate adequate ion supply for redox reactions following circuit switching. The cell was successfully fabricated, followed by the assessment of its discharge characteristics through cyclic voltammetry (CV) and chronopotentiometry (CP) techniques. The cell exhibits an open-circuit voltage of approximately 270 mV and a short-circuit current of approximately 0.30 μA for both circuits 1 and 2. During long-term operation, continuous power generation curves (discharge current: 180 nA) are observed by alternately switching circuits.

2. Materials and methods

2.1. 2D simulation of the discharge process of dual-circuit type STC

To assess the operation of the dual-circuit STC effectively, it is essential to focus on the migration of redox species ions during discharge. A two-dimensional battery model was developed using the simulation software COMSOL Multiphysics (COMSOL Inc., Sweden) to investigate the concentration distribution and diffusion dynamics of ions.

COMSOL Multiphysics offers a range of electrochemical

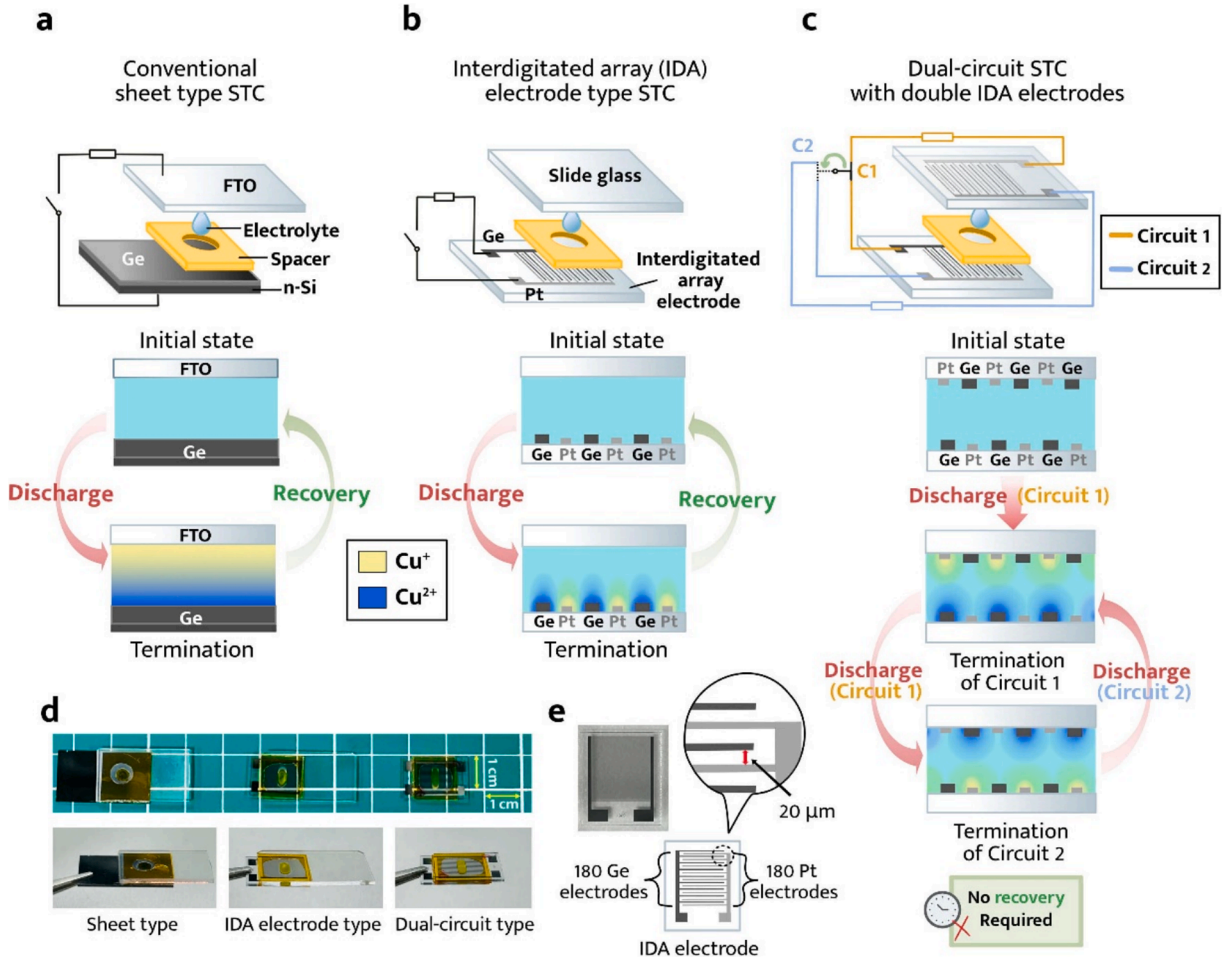

Fig. 2. Structure design principles for dual-circuit STC with no need for recovery time. a, Conventional sheet-type STC. b, Interdigitated array electrode-type STC. c, Dual-circuit STC with double interdigitated array electrodes. d, Digital camera image of the 3 types of fabricated STCs. e, An interdigitated array electrode.

measurement methods, battery models, and analytical tools, which are used for predicting and analyzing experimental results [22–24]. The finite element method (FEM) integrated in COMSOL is particularly suited for studying complex electrochemical systems [25]. This method is advantageous for analyzing complex device geometries and boundaries, making it well-suited for electrode analysis. This approach divides the system into small regions and solves equations by approximating them to simpler forms in each region. Considering the microscale nature of the IDA electrode used in this study (Fig. 2e), employing 2D simulation is suitable because similar models have been successfully applied in previous studies to calculate ion concentration distributions [26].

For this study, a model based on the "Diffuse Double Layer with Charge Transfer" framework in COMSOL's electrochemical module was adopted, integrating electrophoresis and diffusion for mass transport, with the Nernst–Planck equation (3) as the governing equation:

$$J = -D\nabla c - zuFc\nabla\Phi \tag{3}$$

where J is the total flux, D is the diffusion coefficient, ∇c is the concentration gradient, z is the valence of ionic species, u is the velocity vector, F is the Faraday constant, c is the ion concentration, and Φ is the electric potential. Regarding boundary conditions, calculations are performed under specific conditions: the Nernst equation (4) applies at the electrode surface, and the electrode reaction is modeled using the Butler–Volmer rate equation (5):

$$E = E_{eq} - \frac{RT}{nF} ln\prod_i \left(\frac{c_{i,red}}{c_{i,ox}}\right) \tag{4}$$

$$i = i_0\left(\exp\left(\frac{\alpha_a F\eta}{RT}\right) - \exp\left(\frac{\alpha_c F\eta}{RT}\right)\right) \tag{5}$$

where E is the electrode potential, E_{eq} is the equilibrium potential, R is the universal gas constant, T is the temperature in kelvins, n is the number of electrons transferred in the reaction, $c_{i,red}$ and $c_{i,ox}$ are the reduced and oxidized ion concentration respectively, i is the electrode current density, i_0 is the exchange current density, a_a is the anodic charge transfer coefficient (dimensionless), a_c is the cathodic charge transfer coefficient (dimensionless), and η is the activation overpotential.

Fig. 3 illustrates the computational model of the dual-circuit STC (a two-dimensional plane cut from the cross-sectional view), designed based on the IDA electrodes that will be used in the experiment, including their dimensions and spacing. Because the IDA electrodes are all horizontally distributed on the substrate, an appropriate number of bar-shaped electrodes are used to simulate the overall trend instead of including a huge number of the electrodes in the 2D model. During the results analysis, only the central electrodes are observed to minimize the influence of the surrounding electrolyte on ion distribution. The electrodes depicted in Fig. 3 (comprising 4 electrodes on the top and bottom) were organized as a single group, with a total of 5 groups (20 electrodes in total) arranged horizontally in the entire simulation model (Supplementary Fig. 1). In this setup, circuit 1 comprises Ge (Lower) and Pt (Upper), while circuit 2 features Ge (Upper) and Pt (Lower). The discharge reactions for each circuit are depicted below the model, respectively. The entire model was structured as a rectangular domain.

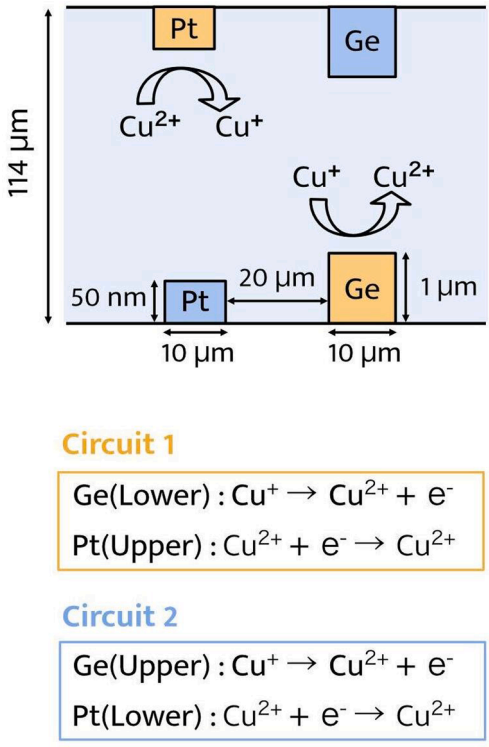

Fig. 3. 2D simulation model of a dual-circuit STC, viewed cross-sectionally.

Apart from the electrodes, the remaining space represented the battery's interior (electrolyte), serving as the computational area. Periodic boundary conditions were applied on the left and right sides of the rectangle using equations (6) and (7).

$$\Phi_{int} = \Phi_{ex} \tag{6}$$

$$c_{int} = c_{ex} \tag{7}$$

This ensures that the electrolyte potential Φ and ion concentration c remain constant at the boundaries where periodic conditions were applied, thereby simulating an infinitely extending periodic structure along the x-axis direction. Additionally, all computational domain boundaries were designated as insulators, restricting ion migration in the computational box.

The mesh was configured into two primary regions. The first region, adjacent to the electrode edges, was set to "extremely fine" according to COMSOL's preset settings, while the remaining region was set to "fine". The ions considered in the electrolyte included Cu^+, Cu^{2+}, Li^+, and Cl^- (key parameters used in the calculations are detailed in Table 1), which were defined by their charge numbers and diffusion coefficients. Since extensive data on the diffusion coefficient of Li^+ under similar conditions is available, these literature values were applied in the model, while Na^+ was used in the experiments. As both NaCl and LiCl serve as supporting electrolytes, this substitution has minimal impact on the visualization of ion concentration distribution and does not significantly affect the model results.

Table 1
Main parameters used in the calculations.

Parameters	Value
Diffusion coefficient in PEG (Cu^+, Cu^{2+})	1.95×10^{-11} (m^2/s) [16]
Diffusion coefficient in PEG (Li^+, Cl^-)	8.90×10^{-11} (m^2/s) [27]
Electrode potential of working electrode (vs. counter electrode)	0.25 (V)
Exchange current density	1.75 (A/m^2)
Bulk concentration (Cu^+, Cu^{2+})	282.5 (mol/m^3)
Bulk concentration (Li^+)	678 (mol/m^3)
Bulk concentration (Cl^-)	1525.5 (mol/m^3)

2.2. Fabrication of dual-circuit Ge-sensitized thermal cell

2.2.1. Electrolyte

Inside the glove box, CuCl, $CuCl_2$, and NaCl electrolytes were prepared at concentrations of 0.25, 0.25, and 0.6 mmol/g, respectively. Polyethylene glycol (PEG) 600 was chosen as the electrolyte solvent for its low volatility and excellent durability [28], ensuring stable performance at high temperatures. Cu^+/Cu^{2+} was selected as the redox ion pair due to its redox potential being close to the valence band of the Ge semiconductor, facilitating smooth oxidation reactions by thermally excited holes [10]. The specific values of the concentrations were chosen to maintain consistency with previous STC studies [29].The components were mixed and heated on a hot plate at 50 °C and 600 RPM for 24 h.

The working electrode Ge is sensitive to moisture [30], and polyethylene glycol (PEG) 600, used as the electrolyte, is hygroscopic. Therefore, the electrolyte preparation was performed in a flow-type glove box under an argon gas atmosphere (with oxygen concentration maintained at 0.2–0.5 ppm) [17].

Before use in the glove box, all reagents underwent vacuum drying at 80 °C for 15 h. Additionally, molecular sieves (Fujifilm Wako Pure Chemical Industries, Ltd.) were heated at 180 °C for 3 h and 350 °C for 4 h in an electric furnace. Subsequently, they were cooled to 50 °C in a vacuum desiccator to remove any residual moisture before adding them to PEG600, which was partially dehydrated to one-third of its original volume.

2.2.2. Electrode pretreatment and cell fabrication

The IDA electrode (Tohnic Corporation, Japan) consists of Ge as the working electrode and platinum (Pt) as the counter electrode, both deposited on a quartz substrate (thickness: 0.525 mm) using an electron beam evaporation system. First, a 20-nm-thick layer of Cr is deposited on the quartz substrate to improve the adhesion of Ge and Pt. Subsequently, Ge (thickness: 1 μm) and Pt (thickness: 0.05 μm) are deposited on top of the Cr layer. Each electrode is 10 μm wide, with a 20 μm distance between the Ge and Pt components. Two IDA electrodes were required for this study, one of which had a lead copper wire soldered to the terminals of Ge and Pt for convenient connection during electrochemical measurements. The flowchart for the fabrication of the dual-circuit STC is shown on Fig. 4.

The two IDA electrodes underwent a cleaning process beginning with ultrasonication in ethanol for 5 min, followed by immersion in ultrapure water at 70 °C for 10 min to remove surface oxide films. Typically, hydrofluoric acid is the standard method for oxide film removal [17]. However, it was avoided here because the thin Ge and Pt layers deposited on the quartz substrate may be damaged or dissolved by it. Instead, a combination of ultrasonic cleaning and high-temperature pure water treatment [31] was employed, which, although less potent than hydrofluoric acid, effectively removed the water-soluble oxide film from the Ge surface to a certain extent.

Next, a double-sided tape (thickness: 114 μm, double-coated Kapton Polyimide Film P-223, Nitto, Japan) with a hole in the middle was affixed to one of the IDA electrodes to serve as a spacer. Subsequently, both IDA electrodes were introduced into the glove box. Then, 1 μL of electrolyte was carefully applied onto the electrode section of the IDA electrode, ensuring it was in the hole of the insulating tape. The Ge and Pt terminals of both sets of comb electrodes (four in total) were left exposed. The second IDA electrode was then positioned face down, covering the bottom electrode so that its surface made contact with the electrolyte. Then, the entire cell was left at room temperature inside the glove box overnight (18 h) before measurement. The thickness of the fabricated cell was measured at three different locations and averaged

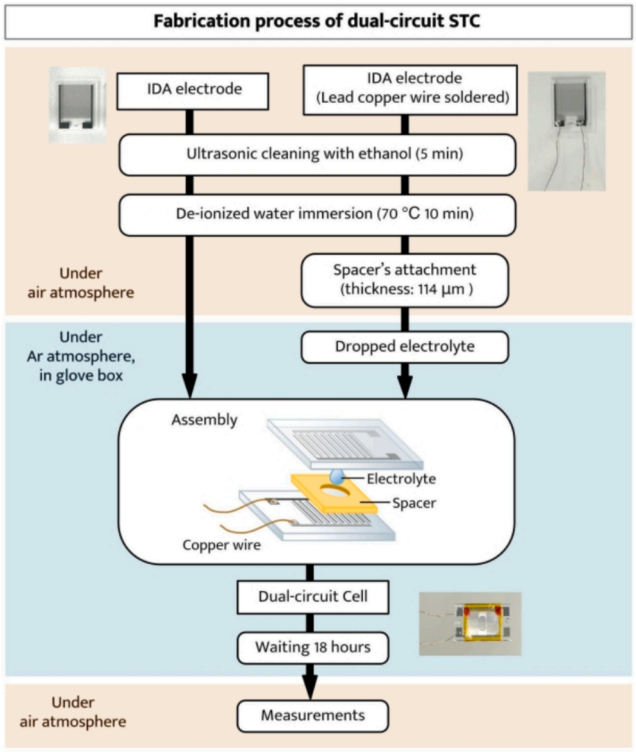

Fig. 4. Flowchart of the dual-circuit STC's fabrication process.

1.182 mm.

2.3. Electrochemical measurements

The assembled dual-circuit STC cell was placed on a hot plate, with Ge connected to the measurement device as the working electrode and Pt as the counter electrode, as depicted in Fig. 5. Electrochemical measurements were conducted at 60 °C, with the cell surface temperature monitored at 54.9 °C using a radiation thermometer.

In addition to open-circuit voltage (OCV) measurements, we primarily used CV to assess power generation capacity and chronopotentiometry (CP) to evaluate long-term discharge performance characteristics. The measurements were performed using a VSP-300 high-performance electrochemical measurement system (6-channel, advanced model, TOYO Corporation). Given the dual-circuit setup, two channels of the measurement system were used.

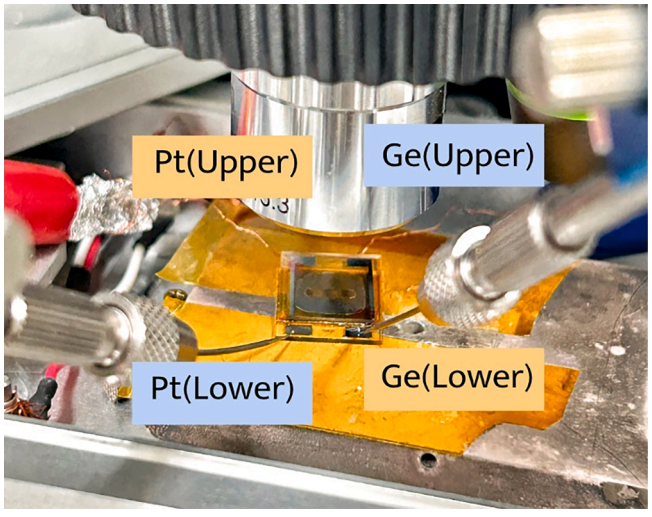

Fig. 5. Measurement setup for the dual-circuit STC, employing both manipulators and alligator clips.

During CV, the voltage sweep was performed from the V_{oc} to 0 V. The response current curve from the third cycle of the voltage swept between the working electrode and the counter electrode was analyzed. The voltage corresponding to zero current was recorded as the V_{oc}, while the current at zero voltage (y-intercept of the plot) was noted as the short-circuit current I_{sc}. CV tests were conducted at a scan rate of 10 mV s^{-1} for all experiments.

In CP, the following procedure was established for the long-term operation measurements of the cells in this system with a discharging current of 180nA. The measurements for each circuit proceeded as follows: (1) CP → (2) OCV → (3) CP. Immediately after completing step (3), the circuit was switched (requiring 1 s), and the other circuit was evaluated using the same procedure: (4) CP → (5) OCV → (6) CP. This circuit switching procedure was repeated 3 times to ensure reproducibility.

3. Results and discussions

3.1. Concentration distribution of Cu^+

The simulation results are illustrated in Fig. 6, showing the concentration distribution of Cu^+ at a specific time through color differentiation. The dynamic concentration map of Cu^+ throughout the entire discharge process is visualized in an animation (Supplementary Animation 1). Additionally, the concentration distribution of Cu^{2+} was also visualized and is presented in Supplementary Animation 2.

In this model, ion transfer analysis was performed over a total period of 600 s. The discharge circuit switches every 200 s, with circuit 1 active during t = 0–200 s and 400–600 s, and circuit 2 active during t = 200–400 s. It is crucial to focus on the change in ion distribution before and after alternating discharge circuits.

Specifically, the results at t = 190 s and t = 210 s (Fig. 6) are examined to illustrate the Cu^+ distribution during the switch from circuit 1 to circuit 2. At t = 190 s, Cu^+ is predominantly produced at the Pt (Upper) electrodes owing to discharge in circuit 1, resulting in a Cu^+-rich upper region of the cell. Concurrently, Cu^+ is consumed at the working electrode Ge (Lower), leading to a significantly lower concentration. In this case, the ion supply may not have adequately sustained the reaction, thereby concluding the discharge process. At t = 210 s, just 10 s after switching the discharge to circuit 2, Cu^+ ions on the upper side were promptly consumed, confirming sufficient ion supply for discharge in circuit 2. Transitioning from circuit 1, which had completed its discharge, to circuit 2 demonstrated the cell's capability to continue discharging.

Moreover, the iterative nature of this process is described below:

circuit 1 discharge → end of circuit 1 discharge
→ circuit 2 discharge → end of circuit 2 discharge
→ circuit 1 discharge…

It indicates the potential for continuous discharge from a single STC without needing recovery time, which can be achieved simply by switching circuits.

However, it is important to note a limitation of this two-dimensional model in the study: it does not account for the chain structure of polymer solvents (PEG600) in the electrolyte and the specific electrode materials. Consequently, the model does not replicate the diffusion behavior of polymer solvents [27] or the unique redox reactions driven by thermally excited electrons in STCs. Also, this model is based on the cross-sectional view of IDA electrodes to observe the ion movement between the working and counter electrodes. The influence of the length of the bar-shaped electrodes on ion movement could not be examined. Thus, this model focuses solely on ion concentration distributions during the initial and near-steady-state phases of the discharge reaction and ion movement immediately before and after changing the discharge circuit. For

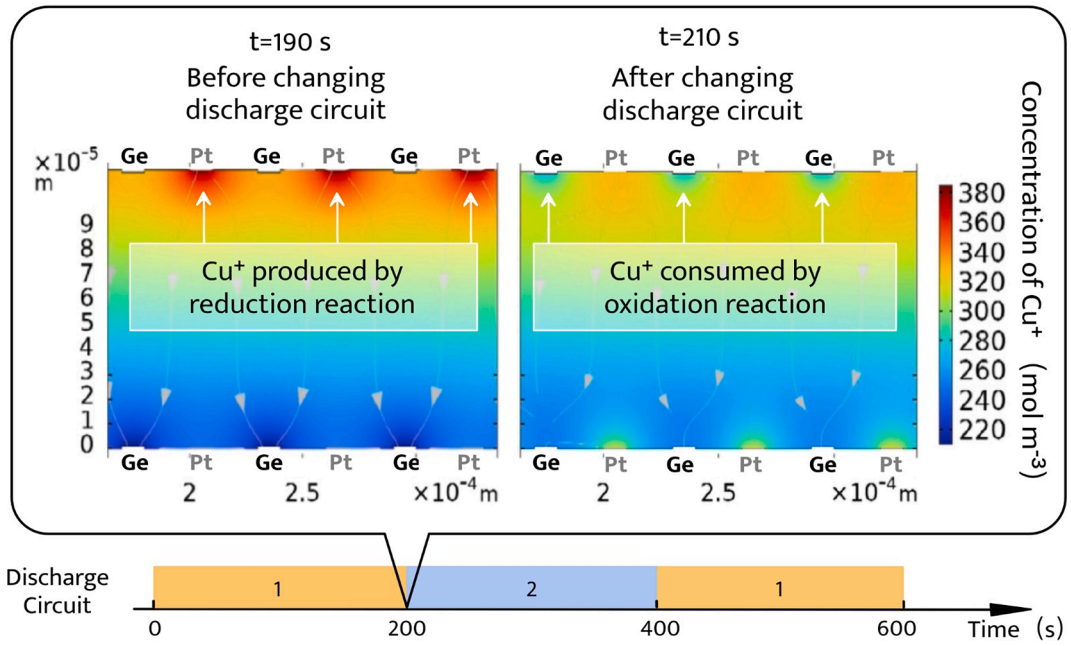

Fig. 6. Concentration map of Cu^+ before and after switching discharge circuits from 1 to 2 at 80℃ (enlarged version of the actual model). At t = 190 s, Cu^+ is primarily produced at the Pt electrodes during discharge in circuit 1, creating a Cu^+-rich upper region while being consumed at the Ge electrode, leading to a lower concentration. At t = 210 s, just 10 s after switching to circuit 2, the red region around the upper electrodes indicates sufficient Cu^+ ions, ensuring a continuous oxidation reaction.

more precise numerical values, employing a three-dimensional model for analysis would be ideal; however, this entails a more complex and time-consuming computational process.

3.2. CV curves

The CV curves for each circuit are depicted in Fig. 7a and 7b. Owing to the inability to simultaneously measure both circuits, CV was first conducted on circuit 1, followed by the measurement on circuit 2.

Additionally, given the thin and delicate structure of IDA electrodes, which may potentially detach, it is crucial to verify the overall stability of the battery. In preliminary experiments, we observed that under long-term operation at 80 °C, the Ge electrode showed delamination (Supplementary Fig. 2), which may prevent the battery from recovering its original V_{oc} and I_{sc} after discharge. This suggests that even at 60 °C, the possibility of electrode delamination must be considered. This issue

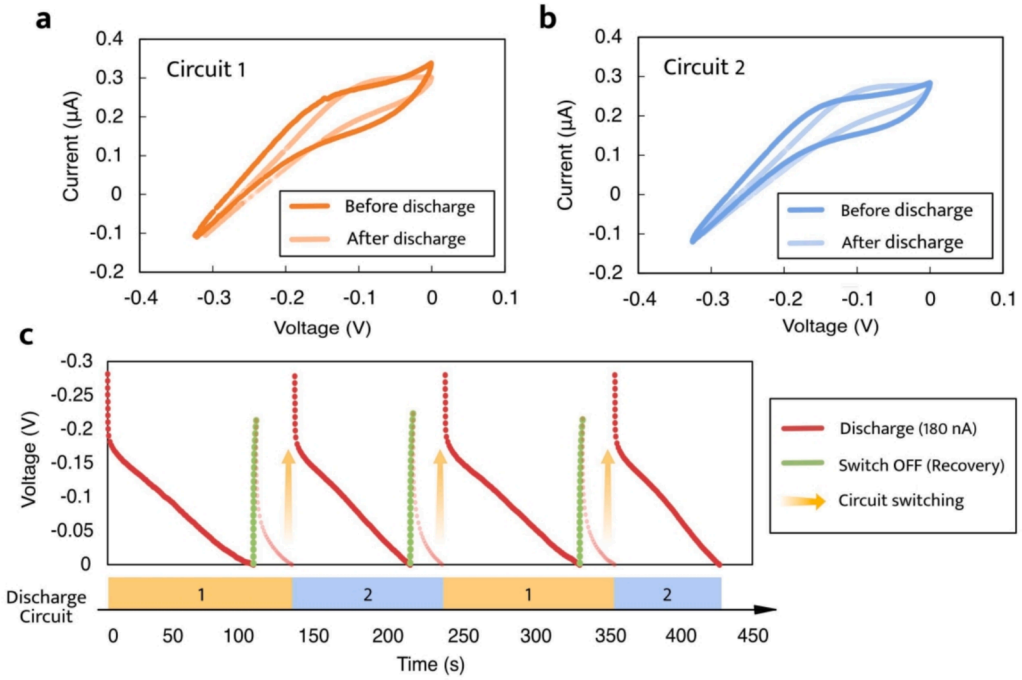

Fig. 7. Electrochemical performance of dual-circuit STC with switching circuit at 60℃. a, CV curves of circuit 1 in the dual-circuit STC (before and after complete discharge measurement, scan rate: 10 mV s^{-1}). b, CV curves of circuit 2 in the dual-circuit STC (before and after complete discharge measurement, scan rate: 10 mV s^{-1}). c, CP curves illustrating circuit switching upon termination of one circuit (switching 3 times, discharging at 180 nA).

possibly arises from the significant difference in thermal expansion coefficients between the Ge electrode and the SiO_2 substrate [32]. The thermal expansion coefficient of SiO_2 is approximately twice that of Ge, and 1 to 1.5 times that of Pt, as well as around twice that of Cr [33]. Cr is used as an intermediate layer to enhance adhesion due to its ability to form chemical bonds with SiO_2. At high temperatures, this mismatch in expansion coefficients inevitably leads to delamination. Based on these findings, it is proposed that modifying the electrode substrate material could significantly enhance the stability of thin-film electrodes. Therefore, following all long-term operation (CP) measurements, CV was again applied to both circuits to assess their performance.

Regarding V_{oc}, results from four measurements across both circuits were consistently approximately −270 mV (circuit 1 before: −277 mV, circuit 2 before: −276 mV, circuit 1 after: −261 mV, circuit 2 after: −262 mV), demonstrating nearly identical values. Similarly, the I_{sc} remained stable at approximately 0.30 μA for all four measurements (circuit 1 before: 0.34 μA, circuit 2 before: 0.28 μA, circuit 1 after: 0.30 μA, circuit 2 after: 0.28 μA). Given the electrolyte area of 0.06 cm^2, this corresponds to a short-circuit current density (Jsc) of 5 $\mu A/cm^2$. Positive currents and negative voltages were observed, confirming electricity generation in both circuits. Moreover, the consistency of I_{sc} and V_{oc} values before and after the long-term operation measurements indicates the overall stability of the entire cell.

Further, achieving a V_{oc} of approximately 270 mV and an I_{sc} of around 0.30 μA (Jsc of 5 $\mu A/cm^2$) demonstrates that the STC device operates within a reasonable range. The open-circuit voltage, determined by the difference between the Fermi level of the working electrode and the redox level of the electrolyte ions, falls within the expected range of 250–350 mV. In the field of isothermal power generation, our results are comparable to recent studies on organic thermoelectric devices. Kondo et al. (2024) [6] reported a V_{oc} of 384 mV and a Jsc of 1.1 $\mu A/cm^2$ in their device, indicating a similar performance level.

3.3. CP curves

The CP curves illustrating the entire discharging process (discharge current: 180 nA) are presented in Fig. 7c. First, the cell discharged using circuit 1 (first red line), followed by a partial recovery of V_{oc} during a 2-s recovery period (first green line). Attempting to redischarge using circuit 1 immediately resulted in a voltage drop (light red line), indicating the discharge termination for circuit 1. However, after an adjustment period equivalent to a 1-s recovery (orange arrow), switching to circuit 2 enabled continuous discharge (second red line). Notably, the 1-s adjustment period did not significantly affect the redischarge characteristics, as evidenced by the difficulty in redischarging even after a 2-s recovery (first green and light red lines). Thus, the discharge curve immediately following circuit switching can be measured right after the previous circuit's termination (disregarding the 1-s delay).

Next, to verify the reproducibility of continuous discharge, circuit switching was performed three times in the sequence: circuit 1 → circuit 2 → circuit 1 → circuit 2. Surprisingly, each time circuits were switched, a continuous discharge curve comparable to the first one was observed immediately afterward. Here, each circuit's discharge time is approximately 100 s, which is relatively short. To rule out the possibility of electrical discharges originating from the electric double layer (EDL), a fitting [34] was performed on the discharge curve. The results indicate that the discharge of the current cell is not solely from the EDL (Supplementary Fig. 3). The short discharge time is attributed to the high current setting, which yields a substantial output but shortens the discharge duration.

Therefore, this study suggests that switching circuits makes continuous discharge without recovery time achievable in the dual-circuit STC.

3.4. Comparison with other types of STC

The three types of STCs mentioned in the introduction were compared based on key performance parameters, including open-circuit voltage (V_{oc}), short-circuit current (I_{sc}), and recovery time, as summarized in Table 2.

Based on the I-V data from the CV measurement, we estimated the power output of the dual-circuit STC to be approximately 0.34 $\mu W/cm^2$ at 60℃. This output is competitive to the performance of the most widely studied thermoelectric generators (TEGs) for low-temperature harvesting, with Luo et al. (2024) [4] reporting that by enhancing material properties, the micro thermoelectric generator (mTEG) achieved an open-circuit voltage of 57 mV and a power density of 315 nW/cm^2. As shown in Table 2, the dual-circuit type is comparable to the other two structures in overall performance but exhibits a decisive advantage in recovery time. While the sheet-type and single-circuit IDA-type still require a switch-off period for recovery, the dual-circuit type enables continuous discharge with no interruption. This is achieved through its circuit-switching mechanism, which allows seamless operation. This feature significantly enhances the practical applicability of the dual-circuit design, making it highly suitable for applications requiring sustained and stable power output.

4. Conclusions

In this paper, there are two design principles for the dual-circuit STC. First, the ion concentration bias resulting from power generation at the upper and lower electrodes is considered, where inadequate ion supply can lead to discharge termination. Second, the microscale distance between Ge and Pt in a single IDA electrode facilitates easy horizontal diffusion of ions on the substrate.

An analysis of ion transfer in the dual-circuit STC electrolyte was conducted using COMSOL, generating outputs for the diffusion and concentration distribution of the redox species Cu^+. The concentration map of Cu^+ confirmed that the ion supply was adequate to maintain redox reactions during circuit switching, demonstrating the potential for continuous discharge in such STCs.

Furthermore, a dual-circuit STC was successfully fabricated using two IDA electrodes to validate the simulation's calculated results in the experiment. The discharge characteristics of the fabricated cell were evaluated using V_{oc}, I_{sc}, and long-term operation measurements, revealing a continuous discharge curve upon switching circuits after one circuit's discharge.

Therefore, future research will focus on the following aspects: (1) Improving electrode stability: The delamination of IDA electrodes could be related to the thermal expansion mismatch between the Ge electrode and the SiO_2 substrate. Modifying the electrode substrate material might help improve stability. (2) Enhancing simulation accuracy: The 2D model used in this study may limit the full understanding of ion movement. Future work will focus on developing 3D simulations to achieve more accurate performance predictions, or refining the 2D simulation

Table 2
Comparison of the different types of STCs.

	Sheet type STC [29]	IDA electrode type STC (single-circuit)	IDA electrode type STC (dual-circuit)
Electrode configuration	Flat sheets substrate	Interdigitated combs	double Interdigitated combs in parallel
Dimensions (length*width*thickness) (mm)	30*15*2	15*10*2	15*10*2
V_{oc} (mV)	230 ± 30 (80 ℃)	225 (60 ℃) 249 (80 ℃)	270 (60 ℃)
I_{sc} (μA)	1.3 ± 0.5 (80℃)	0.6 (60 ℃) 0.9 (80 ℃)	0.3 (60 ℃)
Recovery time	Required (>10 min)	Required (1–2 min)	No need of recovery (<1s)

parameters, such as integrating specific material properties. Additionally, further efforts will be made to explore alternative electrode materials that could provide better thermal stability.

In conclusion, the findings suggest that the dual-circuit STC in this study successfully replicated the simulation results and achieved continuous discharge without recovery time in an isothermal environment through circuit switching. Theoretically, continuous operation is expected by continuously switching circuits. This dual-circuit approach not only enhances the performance of the STC but also opens up new possibilities for battery research, as this structure could potentially be applied to other devices that recycle redox ions and generate electricity through reverse reactions.

CRediT authorship contribution statement

Keting Chen: Writing – review & editing, Writing – original draft, Formal analysis, Data curation. **Mie Tohnishi:** Resources, Methodology. **Akihiro Matsutani:** Supervision, Resources, Methodology. **Sachiko Matsushita:** Writing – review & editing, Validation, Supervision, Resources, Project administration, Methodology, Funding acquisition, Conceptualization.

Declaration of competing interest

The authors declare that they have no known competing financial interests or personal relationships that could have appeared to influence the work reported in this paper.

Acknowledgments

This work was technically and financially supported by Sanoh Co., Japan and Tohnic Co., Japan; technically supported by the Core Facility Center, Science Tokyo., Japan; and financially supported by COI-NEXT (JPMJPF2004), JST SCORE, and KAKENHI (21H02041).

Appendix A. Supplementary data

Supplementary data to this article can be found online at https://doi.org/10.1016/j.enconman.2025.119678.

Data availability

The data supporting the findings of this study are included within the article and its Supplementary Information files. Source data are provided with this paper.

References

[1] The Energy Flow Chart Released by Lawrence Livermore National Laboratory.2022. Available online: https://flowcharts.llnl.gov/ (accessed on 1 May 2024).
[2] Kishore RA, Priya S. A review on low-grade thermal energy harvesting: materials, methods and devices. Materials 2018;11.
[3] Hamid Elsheikh M et al. A review on thermoelectric renewable energy: principle parameters that affect their performance. Renew Sustain Energy Rev 30, 337–355 (2014).
[4] Luo S, Wang C, She Z, Su W, Yan Z. Y-type flexible micro thermoelectric generator using novel encapsulation structure for power enhancement. Energy Convers Manag 2024;301:117950.
[5] Toan NV, et al. Thermoelectric generator using nanoporous silicon formed by metal-assisted chemical etching method. Energy Convers Manag 2025;323:119268.
[6] Kondo S, et al. Organic thermoelectric device utilizing charge transfer interface as the charge generation by harvesting thermal energy. Nat Commun 2024;15:8115.
[7] Matsushita S, Tsuruoka A, Kobayashi E, Isobe T, Nakajima A. Redox reactions by thermally excited charge carriers: towards sensitized thermal cells. Mater Horiz 2017;4:649–56.
[8] Matsushita S, Sugawara S, Isobe T, Nakajima A. Temperature dependence of a perovskite-sensitized solar cell: a sensitized "thermal" Cell. ACS Appl Energy Mater 2018;2:13–8.
[9] Inagawa Y, Isobe T, Nakajima A, Matsushita S. Ag2S-sensitized thermal cell. J Phys Chem C 2019;123:12135–41.
[10] Matsushita S, et al. A sensitized thermal cell recovered using heat. J Mater Chem A 2019;7:18249–56.
[11] Matsushita S, et al. Fermi level dependence of a working electrode on the open circuit voltage in a sensitized thermal cell. Chem Lett 2020;49:1013–6.
[12] Matsushita S. Thermoelectric Power generation element, thermoelectric power generation module including same, and thermoelectric power generation method using same. Japanese Patent PCT/JP2016/075856, 9 (2017).
[13] Sekiya H, Isobe T, Nakajima A, Matsushita S. Can CuFeS2 be used in a sensitized thermal cell? Mater Today Energy 2020;17:100469.
[14] Matsushita S, Tsuruoka A, Kimura Y, Isobe T, Nakajima A. Influence of semiconductor crystallinity on a β-FeSi2 sensitized thermal cell. Solid-State Electron 2019;158:70–4.
[15] Kohata H et al. Power Generation at Room Temperature-How to Design of the Sensitized Thermal Cell; 2021.
[16] Kohata H, et al. Electrolyte thickness dependence upon Ge-sensitized thermal cells. Energy Fuels 2022;36:11619–26.
[17] Ikeda T, et al. Role of the ions in the Ge/(CuCl, CuCl2 and LiCl)/FTO-sensitized thermal cell. J Electroanal Chem 2021;895:115413.
[18] Hasan MN, Nayan N, Nafea M, Muthalif AGA, Mohamed Ali MS. Novel structural design of wearable thermoelectric generator with vertically oriented thermoelements. Energy 2022;259:125032.
[19] O'Regan B, Grätzel M. A low-cost, high-efficiency solar cell based on dye-sensitized colloidal TiO2 films. Nature 1991;353:737–40.
[20] Nazeeruddin MK, Baranoff E, Grätzel M. Dye-sensitized solar cells: a brief overview. Org Photovolt Dye Sensitized Sol Cells 2011;85:1172–8.
[21] Devadiga D, Selvakumar M, Shetty P, Santosh MS. Recent progress in dye sensitized solar cell materials and photo-supercapacitors: a review. J Power Sources 2021;493:229698.
[22] Jokar A, Rajabloo B, Désilets M, Lacroix M. Review of simplified pseudo-two-dimensional models of lithium-ion batteries. J Power Sources 2016;327:44–55.
[23] Moro F, Trovo A, Bortolin S, Del Col D, Guarnieri M. An alternative low-loss stack topology for vanadium redox flow battery: comparative assessment. J Power Sources 2017;340:229–41.
[24] Hussain J, et al. Modeling and simulation of planar SOFC to study the electrochemical properties. Curr Appl Phys 2020;20:660–72.
[25] Gavaghan DJ, Gillow K, Süli E. Adaptive finite element methods in electrochemistry. Langmuir 2006;22:10666–82.
[26] Godino N, Borrise X, Munoz FX, Del Campo FJ, Compton RG. Mass transport to nanoelectrode arrays and limitations of the diffusion domain approach: theory and experiment. J Phys Chem C 2009;113:11119–25.
[27] Diddens D, Heuer A, Borodin O. Understanding the lithium transport within a rouse-based model for a PEO/LiTFSI polymer electrolyte. Macromolecules 2010; 43:2028–36.
[28] Xue Z, He D, Xie X. Poly(ethylene oxide)-based electrolytes for lithium-ion batteries. J Mater Chem A 2015;3:19218–53.
[29] Tamaki K, Matsushita S. Counter electrode dependence of germanium-sensitized thermal cells. Jpn J Appl Phys 2023;63:01SP22.
[30] Bard AJ, Ketelaar J. Encyclopedia of electrochemistry of the elements. J Electrochem Soc 1974;121:212C.
[31] Chui CO, Saraswat KC. Nanoscale germanium MOS dielectrics and junctions. Germanium-Based Technol Ed ES Cor Claeys Elsevier Ltd 2007, 2011,:295–361.
[32] Antonova I, Popov V, Smagulova S, Jedrzejewski J, Balberg I. Charge deep-level transient spectroscopy of SiO2 and Al2O3 layers with embedded Ge nanocrystals. J Appl Phys 2013;113.
[33] Thermal Expansion - Linear Expansion Coefficients. Thermal Expansion - Linear Expansion Coefficients. Available online: https://www.engineeringtoolbox.com/linear-expansion-coefficients-d_95.html (accessed on 4 February 2025).
[34] ISHIKAWA M. Polarization curve and cyclic voltammetry (6) capacitor. Electrochemistry 77, 538–542 (2009).